Faculty and Researchers | Faculty and Researchers' Publications

Deformation and failure of a superplastic AA5083 aluminum material with a Cu addition

Green, W. Paul; Kulas, Mary-Anne; Niazi, Amanda; Oh-Ishi, Keiichiro; Taleff, Eric M.; Krajewski, Paul E.; McNelley, Terry R.

Deformation and Failure of a Superplastic AA5083 Aluminum Material with a Cu Addition

W. PAUL GREEN, MARY-ANNE KULAS, AMANDA NIAZI, KEIICHIRO OISHI,
ERIC M. TALEFF, PAUL E. KRAJEWSKI, and TERRY R. MCNELLEY

A modified AA5083 aluminum sheet material containing a Cu addition of 0.61 wt pct has been investigated under conditions relevant to commercial hot-forming technologies. This material was produced by continuous casting followed by industrial hot and cold rolling into sheet. Deformation and failure mechanisms at elevated temperatures were investigated through mechanical testing, thermal analysis, and microscopy. The effects of Cu addition are evaluated by comparisons with data from AA5083 sheet materials without Cu addition, produced both by continuous and direct-chill (DC) casting techniques. At low temperatures and fast strain rates, for which solute-drag (SD) creep governs deformation, the Cu addition slightly increases tensile ductility at 450 °C but does not otherwise alter deformation behaviors. At high temperatures and slow strain rates, for which grain-boundary-sliding (GBS) creep governs deformation, the Cu addition decreases flow stress and, at 450 °C, improves tensile ductility. A strong temperature dependence for tensile ductility results from the Cu addition; tensile ductility at 500 °C is notably reduced from that at 450 °C. The Cu addition creates platelike particles at grain boundaries, which produce incipient melting and the observed mechanical behavior.

I. INTRODUCTION

THE superplastic grade of aluminum alloy AA5083 is the most common material used for producing parts by superplastic forming (SPF). The ability to make AA5083 behave superplastically is based upon development of a fine grain size, typically less than 10 μm, which is relatively stable at the temperatures typical of SPF operations. Production of such fine recrystallized grain sizes is achieved through large cold-rolling reductions, true strains of -1.3 to -1.6 being typical, and high Mn content, typically from 0.7 to 0.9 wt pct. The high Mn content promotes the formation of intermetallic particles, such as Al_6Mn, in the size range of 1 to 10 μm, which may act to concentrate plastic strain in the adjacent matrix during rolling reduction and serve as nucleation sites for particle-stimulated nucleation (PSN) of recrystallization.[1,2,3] The high Mn content also provides fine precipitates, which act to inhibit grain growth. At the high temperatures and slow strain rates typical of SPF operations, superplastic AA5083 materials deform primarily by grain-boundary-sliding (GBS) creep.[4] The GBS creep provides high strain-rate sensitivity and, with it, a potential for large tensile elongations without the development of flow localization, *i.e.*, necking. When GBS creep controls deformation, the failure of AA5083 materials typically occurs by cavitation.[5–8] However, as strain rate is increased and temperature is reduced, superplastic AA5083 materials transition to deformation controlled by solute-drag (SD) creep.[4] The SD creep provides a lower value of strain-rate sensitivity than does GBS creep, but has an effect sufficient to significantly retard flow localization, providing tensile ductilities of about 200 pct.[5,6,9] The good forming characteristics from SD creep in AA5083 are used in the quick-plastic forming (QPF) process,[10] which is a proprietary variation on SPF developed by General Motors Corp (Detroit, MI). The QPF process produces parts for the automotive industry at significantly lower temperatures and shorter cycle times than traditional SPF processes can achieve.[10]

With the industrial implementation of QPF, superplastic AA5083 materials are now used in the mass production of parts by hot gas-pressure forming. Mass production brings about a new host of material requirements, which were not of primary concern in traditional SPF operations. New requirements include low cost and the ability to form at low temperatures and fast strain rates. The present investigation studies a modified AA5083 material, which is of interest for meeting these new requirements. This material, designated herein as CC-B, is a continuously cast (CC) product that contains an alloying addition of 0.61 wt pct Cu. Continuous casting is a process of interest for reducing the cost of superplastic AA5083 materials. A continuously cast AA5083 material without alloy modification, designated material CC-A, was previously shown to behave differently from materials of nearly identical alloy composition produced by direct-chill (DC) casting.[4,6] The addition of Cu to AA5083 is of interest for two reasons. First, Cu additions have been previously shown by Watanabe *et al.* to lower the flow stress of AA5083 when deformation is by GBS, which was attributed to a reduction in grain size.[11] Second, Cu additions have the potential to provide precipitation strengthening in AA5083 parts produced by QPF and SPF operations, which could improve the moderate strength of recrystallized AA5083 material. The goals

W. PAUL GREEN, Engineer is with Bell Helicopter Textron, Fort Worth, TX 76101. MARY-ANNE KULAS, Engineer, is with the Aerospace Division, Teuchos, 78996 Elancourt, France. AMANDA NIAZI, Graduate Student, and ERIC M. TALEFF, Associate Professor, are with the Department of Mechanical Engineering, The University of Texas at Austin, Austin, TX 78712-0292. Contact e-mail: taleff@mail.utexas.edu KEIICHIRO OISHI, Postdoctoral Researcher, is with the Metallic Nanostructure Group, National Institute for Materials Science, Tsukuba, Ibaraki 305-0047, Japan. PAUL E. KRAJEWSKI, Group Manager, is with the Research and Development Center, General Motors Corp., Warren, MI 48090-9056. TERRY R. MCNELLEY, Professor, is with the Department of Mechanical Engineering, Naval Postgraduate School, Monterey, CA 93943-5146.

of the present investigation are to determine the mechanisms of deformation and failure in material CC-B, compare these with unmodified AA5083 materials previously investigated,[4,6] and determine the effect of Cu on tensile ductility.

II. EXPERIMENTAL PROCEDURE

The alloy composition of material CC-B is given in Table I, along with its sheet thickness and the cold-rolling strain used in its production. Also given are data for two materials studied in previous investigations,[4,6] which are used in this study for comparison with the CC-B material. These include materials CC-A, which is also a continuously cast material, and material DC-C, which was produced by DC casting. Neither material CC-A nor DC-C contains more than trace amounts of Cu. All materials were industrially hot and cold rolled into sheets following casting. Four types of mechanical and thermal tests were conducted on the three AA5083 materials: elongation-to-failure (EF) tests, strain-rate-change (SRC) tests, transient-behavior (TB) tests, and differential-scanning-calorimetry (DSC) tests. In addition, microstructural observations of these materials were made using an optical microscope, a scanning electron microscope (SEM), and a transmission electron microscope (TEM). The results of mechanical tests and some microstructure observations on materials CC-A and DC-C have been previously reported[4,6] and are referenced only for comparison to the data of material CC-B.

The EF, SRC, and TB tests involved straining tensile ''dog-bone'' coupons at a variety of strain rates and temperatures. Tensile coupons had a gage length of 25.4 mm for EF tests and 50.8 mm for SRC and TB tests. All coupons had a gage width of 6 mm, a shoulder radius of 7.9 mm, and a thickness of the as-received sheet material, as given in Table I. All tensile coupons were machined with the long axis, *i.e.,* tensile direction, parallel to the sheet rolling direction. Coupons were held rigidly in shoulder-loading grips, which prevented significant deformation in the grip region, allowing accurate calculation of plastic strain from crosshead displacement measurements. Samples were tested using a computer-controlled, screw-driven testing frame equipped with a three-zone resistance furnace; the three independently controlled heating zones enabled temperature control to within ± 1 °C. Tests were performed at temperatures from 425 °C to 500 °C and at initial true-strain rates ranging from 3×10^{-5} to 6×10^{-2} s^{-1} using constant crosshead speeds.

For EF tests, specimens were pulled in tension until either failure or a specific desired elongation was reached. Elongation-to-failure data were taken at approximate true-strain rates of 3×10^{-4}, 3×10^{-2}, and 6×10^{-2} s^{-1} and at temperatures of 450 °C and 500 °C. The strain rate was kept to within 2 pct of a constant true-strain rate, calculated assuming uniform elongation and conservation of volume, by imposing a series of increasing crosshead speeds, rather than a single, constant crosshead speed. The SRC tests imposed a prescribed series of crosshead speeds, each held for a minimum of 2 pct engineering strain, providing a series of nearly constant true-strain rates, with each achieving an approximately steady-state flow stress. A prestrain of approximately 15 pct engineering strain was initially applied to set the specimen in the grips and stabilize its microstructure. Following this first step, seven sequential steps of increasing strain rate were imposed, with rates varying from 3×10^{-5} to 3×10^{-2} s^{-1}. The SRC tests were conducted at 425 °C, 450 °C, 475 °C, and 500 °C. The steady-state flow stress was measured for each successively applied strain rate. Upon completion of the first seven-step series, two strain-rate steps were duplicated in order to test repeatability of the flow stress measurements; the repeated steps consistently produced very similar results to those of the first series. The TB tests, specialized versions of SRC tests, were conducted at 450 °C. The TB tests imparted a series of large strain-rate increases and decreases, with strain rate held constant after each change for sufficient strain to achieve an approximately steady-state flow stress. Data from TB tests are used to measure flow-stress transients that occur upon strain-rate changes. This testing technique has been previously described in Reference 4.

The DSC process involves measuring the heat flow into or out of a sample as a function of temperature, as the sample is heated or cooled at a constant rate.[12] Differential scanning calorimetry was used to determine recrystallization and melting temperatures of the AA5083 materials. The equipment used for these experiments was a PerkinElmer DSC-7 differential scanning calorimeter (Wellesly, MA). This instrument has a detection limit of 0.002 mW, or about 0.045 μW/mg for the smallest sample mass used, and temperature accuracy to within ± 0.1 °C. Data are reported after compensation for the instrument baseline; a baseline data set was acquired immediately prior to testing of the specimen.[12] In addition to DSC tests of materials CC-A, CC-B, and DC-C, samples of high-purity (99.999 pct) aluminum were tested to establish a reference data set. In producing DSC specimens of each material, disks with a diameter of approximately 6.4 mm were blanked from cold-rolled sheet. These were thinned with SiC papers to fit into high-purity aluminum boats. The DSC tests were conducted using an empty high-purity aluminum boat as a reference specimen. Two specimens were tested for each material: one in the cold-rolled condition (as-received) and

Table I. Thicknesses, *t*, Cold-Rolling Strain, ε_{CR}, Recrystallized Lineal-Intercept Grain Size, *d*, and Compositions in Weight Percent of the Three AA5083 Materials

| Material | *t* (mm) | ε_{CR} | *d* (μm) | Composition (Wt Pct) | | | | | | | | | |
				Si	Fe	Cu	Mn	Mg	Cr	Zn	Ti	Zr	Al
DC-C	1.2	−1.3	6.5	0.15	0.20	0.03	0.76	4.50	0.07	0.02	0.01	—	bal
CC-A	1.0	−1.6	8.0	0.07	0.22	0.02	0.72	4.70	—	—	—	<0.01	bal
CC-B	1.0	−1.4	6.9	0.09	0.18	0.61	0.71	4.70	—	—	—	<0.01	bal

the second after a recrystallization heat treatment. Typical recrystallization heat treatments involved soaking at a temperature of 450 °C for 30 minutes, after which specimens were immediately quenched in water. All samples were sealed in stainless-steel foil during this heat-treating procedure. The DSC heating schedule included an initial 3-minute soak at 25 °C, followed by controlled heating of both sample and reference to 580 °C at a constant rate of 10 °C/min. For most experiments, data acquisition was terminated after reaching 580 °C, and the specimen was returned quickly to room temperature. For one experiment on material CC-B, the specimen was heated to 580 °C and was subsequently cooled at a rate of 10 °C/min to a temperature of 25 °C.

A metallographic sample of alloy CC-B was taken from the undeformed grip region of a SRC specimen tested at 450 °C to measure the statically recrystallized grain size. The sample was aged at 150 °C for 24 hours to sensitize grain boundaries for chemical attack and was then polished and immersed in a solution of 10 pct phosphoric acid at 50 °C with mild agitation to preferentially etch grain boundaries. Specimens thus prepared were examined in an optical microscope bright field. A minimum of five images for grain-size measurement was digitally acquired at 500 times magnification and a digital resolution of 0.16 μm/pixel. Images were analyzed manually using the ASTM E112 standard[13] to measure lineal-intercept grain size, which is reported in Table I. Cavity area fractions were measured in tested specimens as a function of strain using optical micrographs of polished, but unetched, specimens digitally acquired at a magnification of 200 times and a digital resolution of 0.5 μm/pixel. These images were analyzed for cavity area fraction using the ImageJ software package.[14] Particle-size population densities of intermetallic particles were measured in a similar fashion from undeformed and unetched metallographic specimens, but using an optical magnification of 500 times and digital image resolution of 0.2 μm/pixel. From these images, particle size was measured as equivalent spherical diameter. The failure surfaces and cavities on the surfaces near the failure region of tested specimens were examined using an SEM. Specimens from recrystallized materials were observed in a TEM equipped with an energy-dispersive spectroscopy (EDS) system. Specimens were prepared for TEM observations using standard metallographic grinding and polishing techniques, with final specimen thinning performed by a twin-jet polisher.

III. RESULTS AND DISCUSSION

A. Deformation Mechanisms

Data from SRC tests of the CC-B material are reported in Figure 1(a) as a plot of the logarithm of true-strain rate against the logarithm of modulus-compensated, steady-state flow stress. Modulus compensation of flow stress was accomplished using a quadratic fit[4] to the data of Köster[15,16] for the dynamic Young's modulus, E, of pure Al; the effect of Mg on elastic modulus is negligible.[17] The slope of the data in Figure 1(a) is equal to the stress exponent, n, from the phenomenological equation for creep,[18]
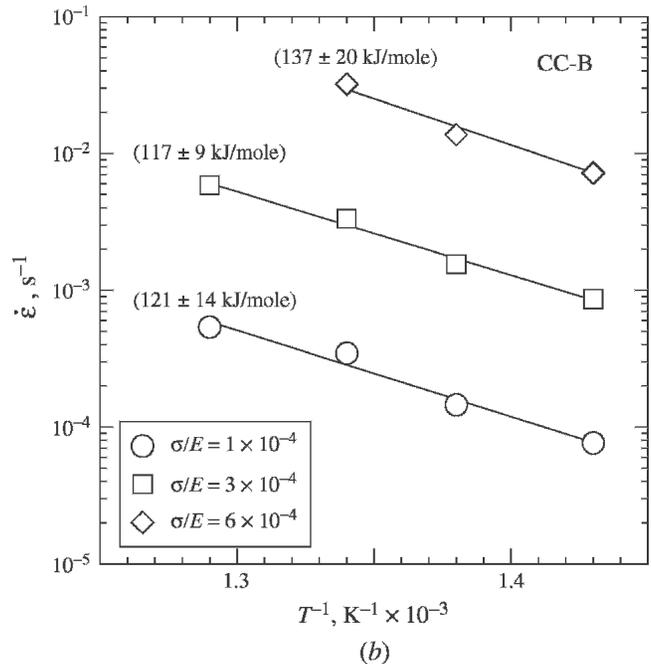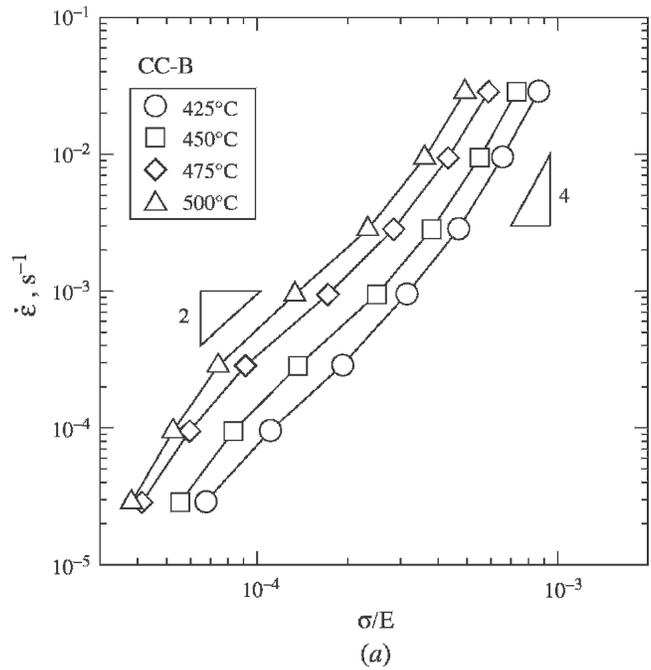

Fig. 1—(a) Data from SRC tests on material CC-B at four different temperatures are plotted as the logarithm of strain rate against the logarithm of modulus-compensated stress. (b) Calculations of the activation energies for creep from the data in (a) are presented at three values of σ/E; calculated values are shown in parentheses next to the corresponding data.

$$\dot{\varepsilon} = A \left(\frac{b}{d}\right)^p \left(\frac{\sigma}{E}\right)^n \exp\left(-\frac{Q_c}{RT}\right) \qquad [1]$$

where $\dot{\varepsilon}$ is true-strain rate, A is a constant that depends on the material and the dominant deformation mechanism, b is the magnitude of the Burgers vector, d is the grain size, p is the grain-size exponent, σ is the steady-state true flow stress, Q_c is the activation energy for creep, R is the

universal gas constant, T is absolute temperature, and the remaining terms are as previously defined. The data of Figure 1(a) indicate a stress exponent of $n \approx 4$ at high stresses and fast strain rates, which is consistent with deformation by SD creep in commercial 5000-series Al alloys.[4,9,19] A value of $n \approx 2$ is indicated at low stress and slow strain rates, which is consistent with deformation by GBS creep.[4,18] At the slowest rates and highest temperatures, n again increases, which is likely indicative of a moderate threshold-stress behavior, as has been observed in other superplastic AA5083 materials.[4] The threshold stress is measured to be approximately 0.9 MPa by using the graphical method of Lagneborg and Bergman,[20] assuming a stress exponent of 2. The data of Figure 1(a) were used to calculate creep activation energies at three values of σ/E. These calculations are represented graphically in Figure 1(b), on which activation energy for creep is proportional to the slope of the data, as given by the relation

$$Q_c = -R \frac{\partial \ln \dot{\varepsilon}}{\partial 1/T}\bigg|_{\sigma/E} \qquad [2]$$

It is of note that the smallest value of σ/E at which activation energy is calculated, 10^{-4}, is above the values for which threshold stress has a significant effect (Figure 1(a)). As a result, the effect of threshold stress on the calculation of activation energies in Figure 1(b) is negligible; the effect is less than the reported measurement errors. Calculated activation energies for creep are indicated in Figure 1(b), along with the standard errors of their calculation, and vary from $Q_c = 137$ kJ/mole at the highest σ/E to 117 and 121 kJ/mole at the lower σ/E values. The high value of $Q_c = 137$ kJ/mole is consistent with the average Q_c value of 130 kJ/mole measured for several other AA5083 materials in the SD creep deformation regime.[4] This value is consistent with the theory of SD creep,[21,22] which indicates that Q_c should equal the activation energy for Mg diffusion in Al, approximately 136 kJ/mole. The low Q_c values of 117 and 121 kJ/mole are consistent, to within the measurement errors noted in Figure 1(b), with the average value of approximately 110 kJ/mole previously measured in the GBS creep regime for a number of AA5083 materials produced by both CC and DC casting methods.[4]

The Zener–Hollomon parameter, $Z = \dot{\varepsilon} \exp(Q_c/RT)$, is used to compare the deformation behavior of material CC-B with those of materials DC-C and CC-A over a wide range of temperatures and strain rates. Figure 2 provides SRC test data from these materials on a plot of the logarithm of Z against the logarithm of σ/E. Because these data transition between deformation by SD creep and by GBS creep, based upon data previously reported for several superplastic AA5083 materials,[4] two activation energies are used in calculating Z. For $\sigma/E < 3 \times 10^{-4}$, deformation is dominated by GBS creep, and a value of $Q_c = 110$ kJ/mole is used. For $\sigma/E > 3 \times 10^{-4}$, deformation is dominated by SD creep, and a value of $Q_c = 136$ kJ/mole is used. In the SD creep regime ($\sigma/E > 3 \times 10^{-4}$), data from materials CC-A and CC-B overlay the same line. These CC materials are slightly weaker than the DC-C material in this regime. The behavior of material CC-B is consistent with the
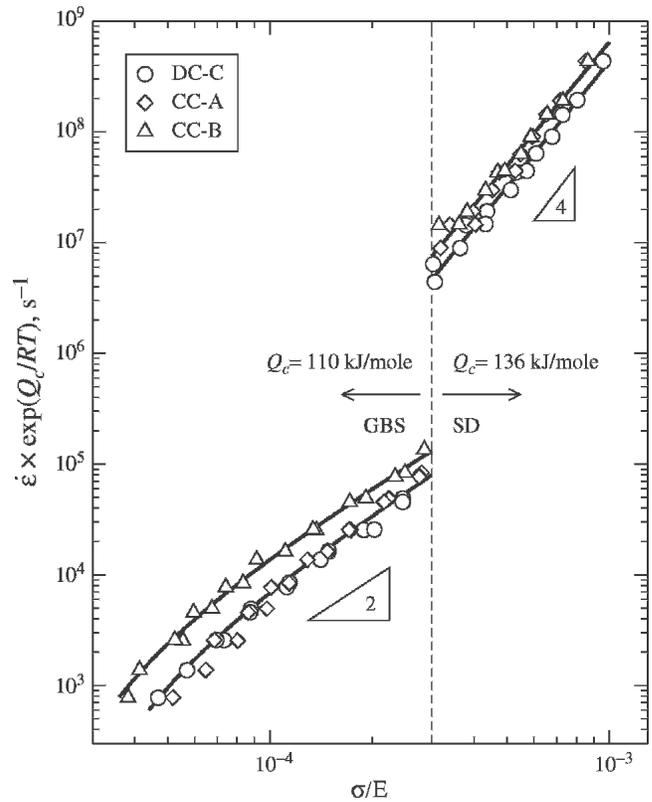

Fig. 2—SRC data from three AA5083 materials are plotted as the logarithm of the Zener–Hollomon parameter vs the logarithm of modulus-compensated stress. For $\sigma/E < 3 \times 10^{-4}$, for which GBS creep dominates deformation, an activation energy for creep of 110 kJ/mole is used. For $\sigma/E > 3 \times 10^{-4}$, for which SD creep dominates deformation, an activation energy for creep of 136 kJ/mole is used.

behavior previously observed for material CC-A in relation to DC cast AA5083 materials[4]; no effect of the Cu additions to material CC-B is evident from Figure 2 in the SD creep regime. In the GBS creep regime ($\sigma/E < 3 \times 10^{-4}$), the CC-B material is significantly weaker than, $i.e.,$ creeps faster than, either the CC-A or DC-C materials. Both the CC-A and DC-C materials exhibit very similar strengths in this regime. The grain sizes reported in Table I indicate that the low flow stress of the CC-B material cannot be explained by grain size alone.

Figure 2 shows the steady-state creep behavior of materials CC-B and CC-A to be very similar in the SD creep regime. It is also of interest to identify any differences in the transient creep responses of these materials in the SD creep regime; stress transients under GBS creep are negligible. Figure 3 presents data from a typical TB test for material CC-B at 450 °C. These data are for a rate increase from 3×10^{-3} s^{-1} to 3×10^{-2} s^{-1}, followed by a decrease back to 3×10^{-3} s^{-1}. The stress transient after each rate change is an inverse creep transient characteristic of SD creep.[4,23] The stress transients are fit using the following equation:[4]

$$\sigma_2(\varepsilon) = \Delta\sigma \, \exp\left(-\frac{\varepsilon}{\tau}\right) + \sigma_{ss,0} \exp\left(-\frac{\varepsilon}{n}\right) \qquad [3]$$

in which σ_2 is the flow stress after the rate change, referenced to a strain of $\varepsilon = 0$ at the rate change; $\Delta\sigma$ is the
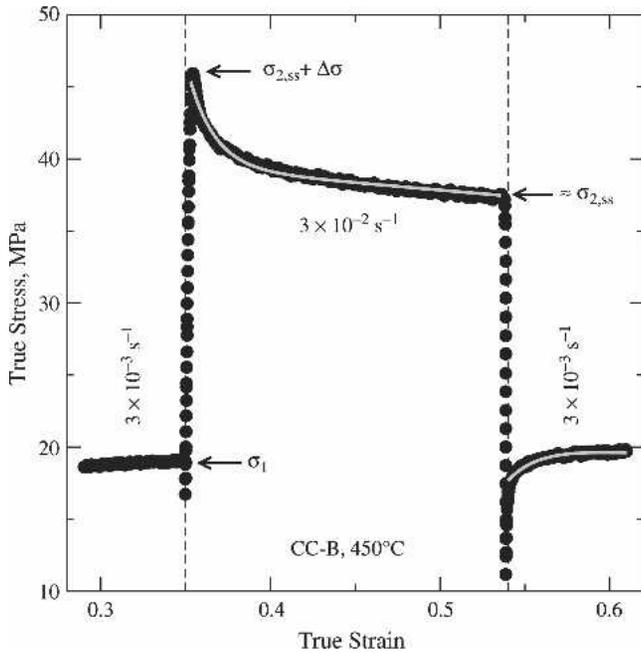
Fig. 3—Data from a TB test of material CC-B at 450 °C are shown within a range of strain rates for which SD creep dominates deformation.

Table II. Transient Behavior Parameters Determined for Material CC-B Tested at 450 °C

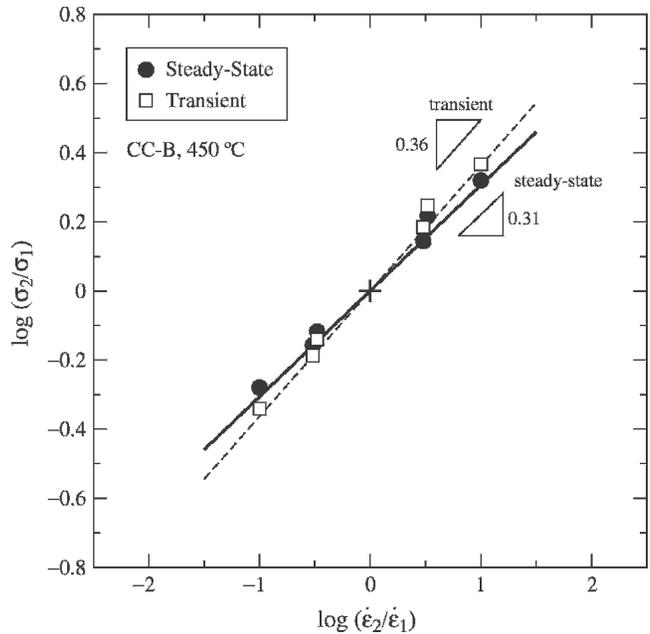| $\dot{\varepsilon}_1$ (s^{-1})	σ_1 (MPa)	$\dot{\varepsilon}_2$ (s^{-1})	$\sigma_{ss,SRC}$ (MPa)	$\sigma_{ss,0}$ (MPa)	$\Delta\sigma$ (MPa)	τ
3×10^{-3}	17	1×10^{-2}	29	28	2.0	0.012
3×10^{-3}	17	1×10^{-2}	29	28	2.1	0.011
1×10^{-2}	28	3×10^{-2}	38	39	3.9	0.013
3×10^{-3}	19	3×10^{-2}	38	39	5.7	0.016
3×10^{-3}	20	3×10^{-2}	38	40	6.0	0.012
1×10^{-2}	28	3×10^{-3}	20	19	−1.3	0.011
3×10^{-2}	38	1×10^{-2}	29	29	−1.5	0.024
1×10^{-2}	28	3×10^{-3}	20	20	−1.3	0.012
3×10^{-2}	37	3×10^{-3}	20	20	−2.7	0.014
3×10^{-2}	38	3×10^{-3}	20	20	−3.1	0.013

Fig. 4—Transient data from material CC-B within the SD creep regime are shown using the graphical construction described in Reference 4.

magnitude of the stress transient; τ describes the rate of exponential decay of the transient; and $\sigma_{ss,0}$ is the steady-state flow stress at the new rate. The last exponential term in Eq. [3] is a correction factor that accommodates for the tests being conducted at constant crosshead speed instead of constant true-strain rate. The value of n in the correction factor is taken from SRC test data, and the correction is rather small for the experiments conducted. The use of Eq. [3] has been described in some detail for a previous investigation.[4] Results from fitting Eq. [3] to CC-B data of several TB tests conducted within the SD creep regime are reported in Table II. In this table, $\dot{\varepsilon}_1$ is the true-strain rate prior to the rate change, σ_1 is the steady-state flow stress prior to the rate change, and $\dot{\varepsilon}_2$ is the true-strain rate following the rate change. It is of note that the steady-state flow stress fit using Eq. [3], $\sigma_{ss,0}$, is very close to that from SRC test data, $\sigma_{ss,SRC}$, for every data set, which provides some confidence in the fit results.

Representation of the transient data of Table II is accomplished in Figure 4 using a graphical construction proposed and discussed in detail for previous investigations.[4,24] In summary, Figure 4 presents data as the logarithm of the ratio of stresses after and before rate changes against the logarithm of the ratio of true-strain rates after and before rate changes. Two fit lines are produced using these data: a steady-state line and a transient line. For the steady-state line, the steady-state values of σ_2 and σ_1 are plotted. For the transient line, the largest stress difference after the rate change is plotted, *i.e.*, $\sigma_2 = \sigma_{ss,0} + \Delta\sigma$. Figure 4 indicates that the transient line is rotated counterclockwise from the steady-state line, which is a characteristic of inverse-creep transients under SD creep. The angle of this rotation is 2.9 deg, which is similar to the value of 2.6 deg previously measured for transient data from materials CC-A and DC-C.[4] The slope of the steady-state line, which is equal to the strain-rate sensitivity ($m = 1/n$), is 0.31, with a stand-

ard error in its measurement of 0.02. The slope of the transient line for material CC-B is 0.36, also with a standard error in measurement of 0.02. These values are similar to those previously measured for the CC-A and DC-C materials.[4,24] The data indicate that the Cu addition in the CC-B material does not significantly alter stress transient behaviors within the SD creep regime.

B. *Tensile Ductility*

Tensile-ductility data from EF tests are presented in Figure 5 as plots of tensile elongation, e_f, against the logarithm of Z. In constructing Figure 5, an activation energy of $Q_c = 110$ kJ/mole was used to calculate Z across data from both the GBS and SD creep regimes. This approximation of using a single Q_c value provides a reasonable temperature normalization for data across both creep mechanisms, without introducing any inconvenient discontinuities in Z, because of the relatively small differences in activation energies between the GBS and SD creep mechanisms in AA5083 materials,[6] and this value of Q_c is used
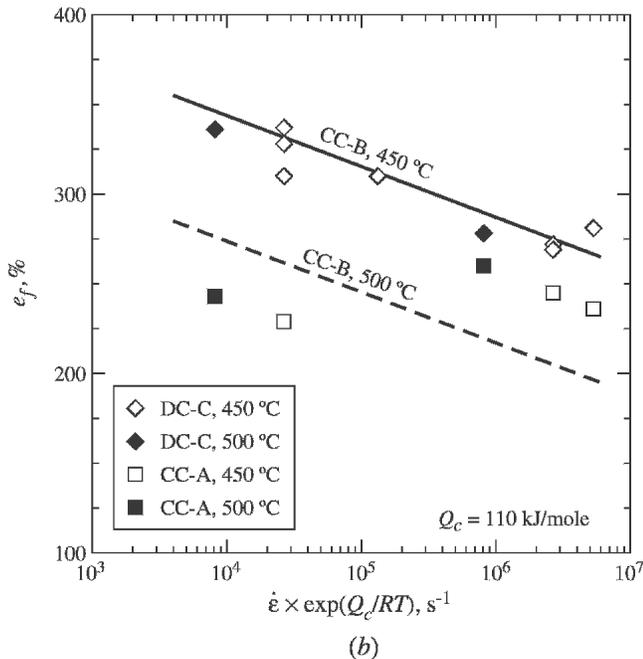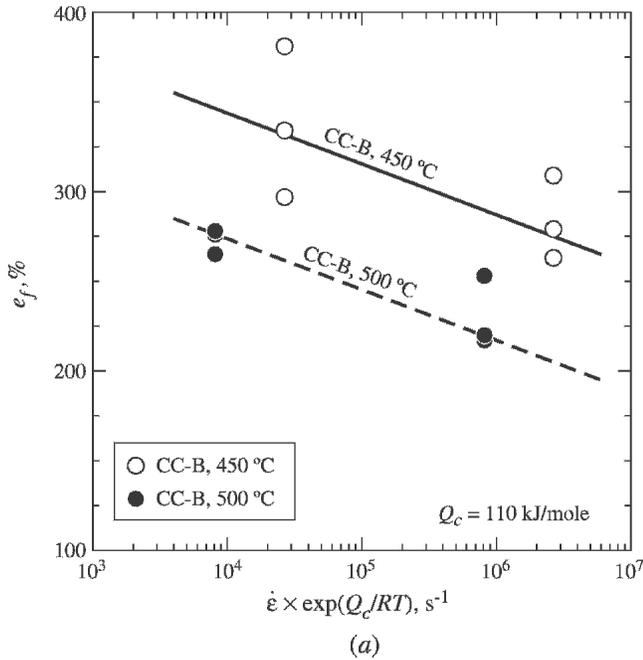
(a)

(b)

Fig. 5—EF data are plotted as a function of the logarithm of the Zener–Hollomon parameter, assuming $Q_c = 110$ kJ/mole, for (a) material CC-B and (b) materials DC-C and CC-A. Fit lines for data in (a) are repeated and in (b) are for comparison between the materials.

Fig. 6—The Q parameter is plotted against the logarithm of the Zener–Hollomon parameter, assuming $Q_c = 110$ kJ/mole, for the three AA5083 materials.

in all subsequent presentations of calculated Z values. Figure 5(a) presents data from the CC-B material, which indicate two important behaviors. First, tensile ductility increases with decreasing Z, which is a characteristic previously observed for AA5083 materials with good forming behavior.[6] Second, the data at 500 °C have a notably lower tensile ductility than do the data at 450 °C, but retain a similar slope. Such a variation of tensile ductility with temperature was not observed previously in either CC- or DC-cast AA5083 materials without Cu addition.[6] For
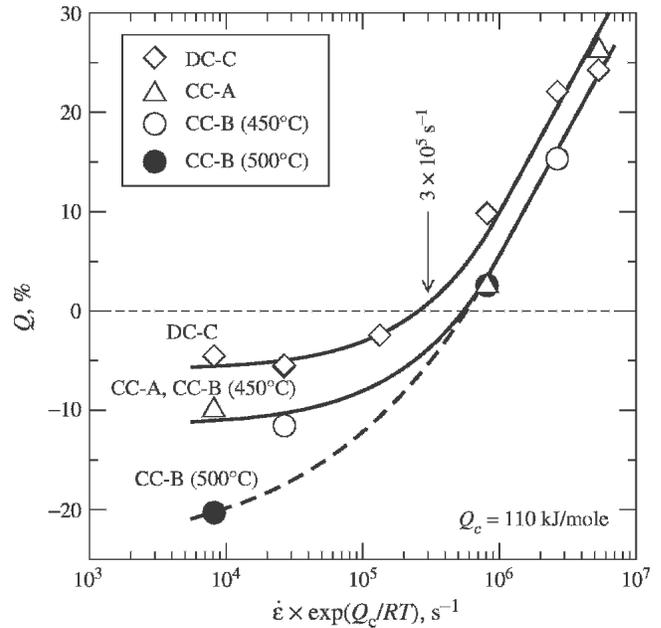
comparison, fits to the CC-B data in Figure 5(a) at 450 °C and 500 °C are repeated in Figure 5(b), which contains data from the CC-A and DC-C materials. The DC-C data overlay the CC-B 450 °C fit line at temperatures of both 450 °C (open symbols) and 500 °C (filled symbols). The data in Figure 5(b) for material CC-A exhibit a different behavior, with elongation decreasing at low Z values. In particular, the ductility of the CC-A material under GBS creep is equal to or less than that under SD creep. This is a result of early cavitation in the GBS regime and is a cause of poor forming behavior.[6] However, this trend in the CC-A material is consistent between data at both 450 °C and 500 °C. It can be concluded that only the Cu-containing CC-B material exhibits a significant difference in elongation behaviors, in relation to Z, between 450 °C and 500 °C.

C. Failure Mechanisms

In order to better understand the nature of failure in the CC-B material, Figure 6 presents a plot of the Q parameter against the logarithm of Z, again using the approximate single Q_c value of 110 kJ/mole. The Q parameter was presented and discussed in detail in a previous investigation.[6] In summary, the Q parameter represents the difference between measured reduction-in-area at failure, q, and the ideal neck-free, cavitation-free reduction-in-area calculated from measured tensile elongation at failure, $q^* = e_f/(1 + e_f)$, as follows:

$$Q = \frac{q - q^*}{q^*} \qquad [4]$$

A Q parameter value significantly greater than zero indicates that failure is dominated by neck development. A Q-parameter value of zero or less indicates that failure is primarily controlled by cavitation growth and interlinkage. Negative values of Q parameter indicate that volume is not

conserved, *i.e.,* cavitation occurred, with Q parameter becoming more negative as the extent of cavitation increases. The controlling failure mechanisms in AA5083 were previously shown to be neck development, when deformation is by SD creep, and cavitation, when deformation is by GBS creep[6]: The Q parameter was found useful for tracking these changes in failure mechanisms of AA5083 materials across a range of hot deformation conditions.[6] The data in Figure 6 for material CC-B are consistent with those results. Data reported previously for materials CC-A and DC-C are reproduced in Figure 6 for comparison with the data of material CC-B.[6] The CC-B data match the results of material CC-A in the SD creep regime ($Z > 3 \times 10^5$ s^{-1}, approximately) and are close to those of the DC-C material. However, the CC-B data are quite different in the GBS creep regime ($Z < 3 \times 10^5$ s^{-1}, approximately). Under GBS creep, the Q-parameter value of material CC-B at 450 °C matches data from material CC-A at both 450 °C and 500 °C. However, the Q-parameter value of material CC-B at 500 °C falls well below data from the other materials at similar Z values. This indicates severe cavitation at failure in material CC-B tested at 500 °C, and this is consistent with the reduction in tensile ductility observed for material CC-B in Figure 5(a) as temperature is increased from 450 °C to 500 °C.

The evolution of cavitation with strain at 450 °C is evaluated by measuring cavity area fraction in specimens deformed in tension to a variety of strains, which were calculated from local area-reduction measurements. The results of these measurements are reported in Figure 7 as the logarithm of cavity area fraction *vs* true strain for (a) tests in the SD creep regime and (b) tests in the GBS creep regime. Data from the SD creep regime, shown in Figure 7(a), indicate that cavitation in material CC-B develops with strain in the same manner as in the CC-A material. The rate of cavitation growth with strain, *i.e.,* the slope of the data, is similar between the three AA5083 materials of Figure 7(a), but the CC materials develop significant cavitation at earlier strain than does the DC-C material. This is consistent with differences previously reported between the CC-A and DC-C materials.[6] In the GBS creep regime (Figure 7(b)), the CC-B data have tremendous scatter, as do the CC-A data. Such scatter was not observed in DC-cast AA5083 materials previously investigated.[6] Nevertheless, the CC-B data under GBS creep are quite similar to those of the CC-A material. Any differences between the CC material data sets appear to be within their large scatters. Fits to these data, shown in Figure 7(b), indicate a lesser slope for the CC materials than for the DC-C material. Given the large scatters in data from the CC materials, it is likely wise not to draw conclusions from this difference in slopes. It is, however, clear from Figure 7 that the CC-A and CC-B materials experience significant cavitation at much lower strain than does the DC-C material in either deformation regime. An important conclusion can be drawn from the data in Figure 7 concerning the two CC materials; under GBS creep at 450 °C, cavitation progresses similarly with strain in both the CC materials. Cavity contents of 2 pct and greater generally degrade the mechanical properties of a formed part. Figure 7, thus, indicates that both CC materials may have similar usable forming strains, based upon a maximum allowable cavity content. This is in spite
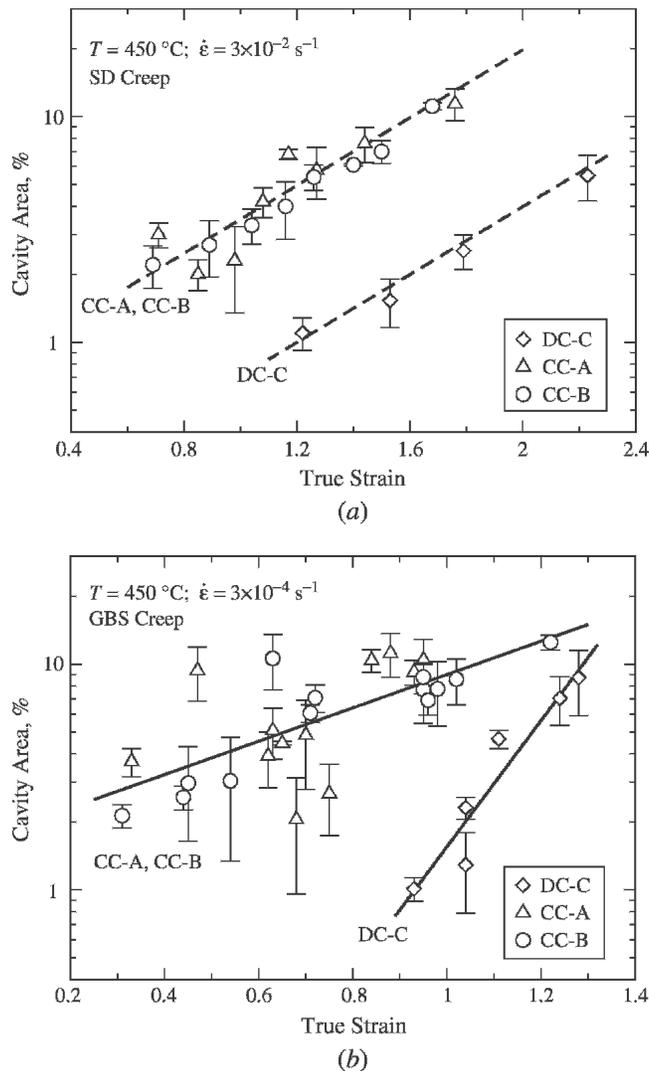

Fig. 7—The logarithm of the cavity area fraction is plotted as a function of true strain under conditions for which (*a*) SD creep and (*b*) GBS creep dominate deformation.
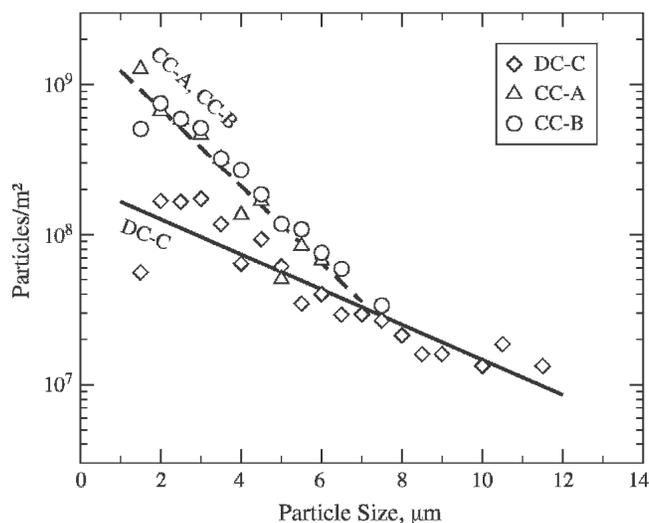

Fig. 8—Intermetallic particle-size population densities in materials DC-C, CC-A, and CC-B are shown.

of data in Figure 5(b), indicating larger tensile ductility at final failure for material CC-B than for material CC-A. Note that the data of Figure 7 were all acquired at a temperature of 450 °C, which eliminates the complication of the temperature effect on ductility shown for material CC-B in Figure 5(a).

A previous study of differences in tensile ductility and cavitation evolution on DC-cast AA5083 materials correlated these differences to a difference in intermetallic particle-size population densities in the range of 1.5 to 7 μm.[5,6] The intermetallic particle-size population density of material CC-B is shown in Figure 8 along with data

previously reported for materials CC-A and DC-C. The CC-B data lay on the same line as the CC-A data, and both CC materials contain a larger population density of fine particles than does the DC-C material. Figure 8 indicates that, for the range of particle sizes evaluated, there are no significant differences in particle-size population densities between the CC materials. Thus, intermetallic particle size distribution does not explain the performance differences between the CC materials.

Previous investigation of the fracture surfaces and open surface cavities near the failure regions of AA5083 materi-
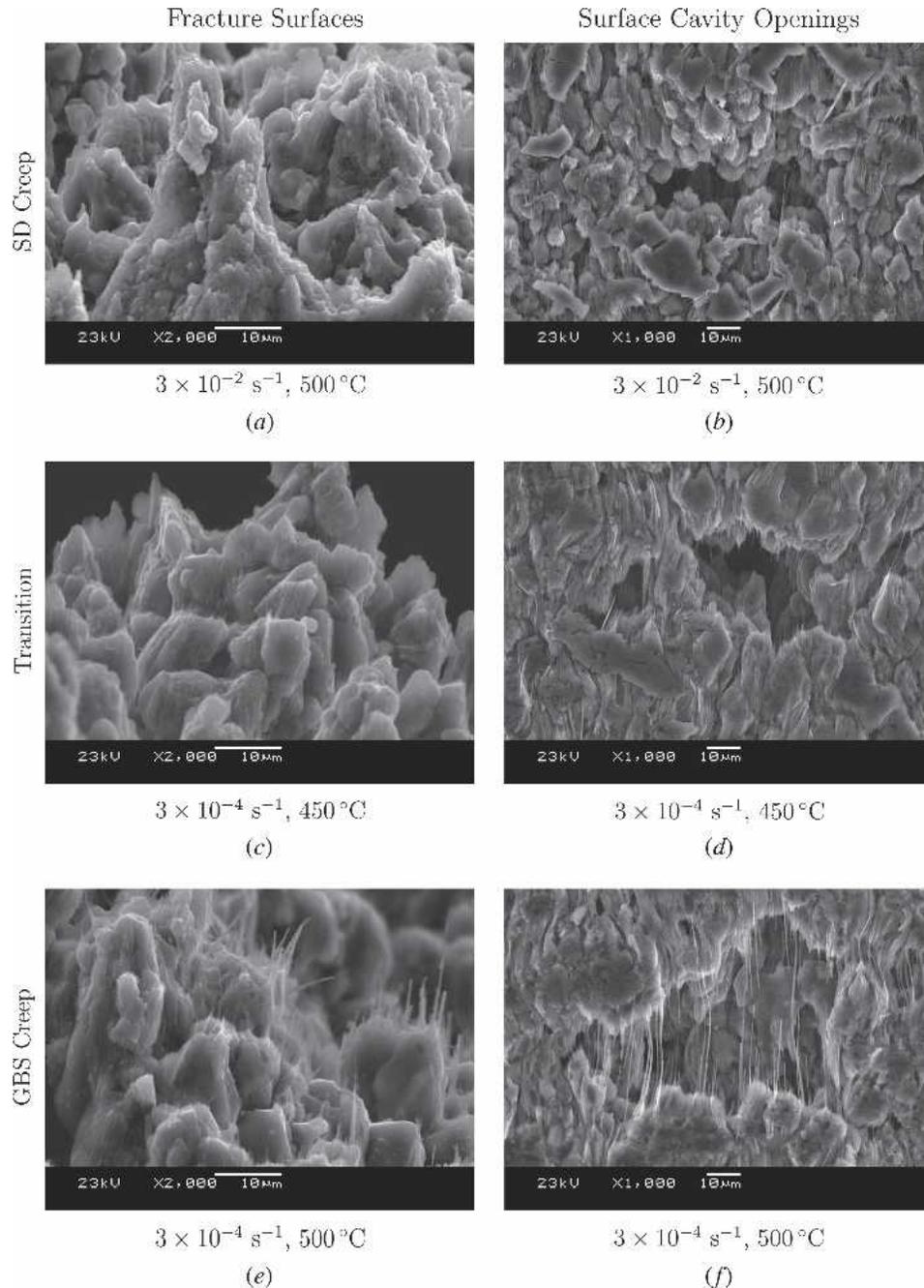

Fig. 9—A series of photomicrographs from the failure regions of material CC-B specimens is shown illustrating the transition from SD creep to GBS creep. The left column shows fracture surfaces formed under (a) SD creep, (c) the transition from GBS to SD creep, and (e) GBS creep conditions. The right column shows surface cavity openings formed under (b) SD creep, (d) the transition from GBS to SD creep, and (f) GBS creep conditions. The tensile axis is approximately vertical for each image.

als revealed a change in failure morphology upon the transition from necking-controlled failure under SD creep to cavitation-controlled failure under GBS creep.[6] Similar failure morphologies are observed for the CC-B material, as shown in Figure 9 for failure surfaces and surface cavities formed under SD creep, (a) and (b), the transition from SD to GBS creep, (c) and (d), and under GBS creep, (e) and (f). Under SD creep, failure surfaces exhibit large local plasticity and deformation structure elongated along the tensile axis. Under GBS creep, failure surfaces exhibit submicrometer-diameter fibers along the tensile axis, which may be characteristic of failure at grain boundaries by local grain-boundary plasticity.[6] At the transition between these two mechanisms, as shown in Figures 9(c) and (d), the failure surfaces exhibit a mix of both feature types, with fewer submicrometer fibers than for the case of deformation under GBS creep. Consistent with previous observations of AA5083 materials,[6] the observation of fibers correlates with deformation, failure, and mechanism transition and not strictly temperature or rate changes. Submicrometer fiber formation at the failure surfaces of the CC-B material is very similar to that previously observed in the CC-A and DC-C materials.[6] No change in behavior from the Cu addition to material CC-B is apparent.

D. *Thermal Analysis and Microstructure*

Data from DSC experiments are reported in Figure 10 for high-purity aluminum and materials DC-C and CC-A in both the cold-rolled and recrystallized states and for material CC-B in the recrystallized state. Data from material CC-B in the cold-rolled state are not reported, but are similar to those of the other AA5083 materials reported in Figure 10 with regard to the observed recrystallization temperature. The high-purity aluminum curves (Figure 10(a)) give no indication of melting within the range of temperatures examined. Data from the AA5083 materials of Figure 10, in both the cold-rolled and recrystallized states, indicate melting at the solidus temperature documented for AA5083 materials, 574 °C[25]; this temperature is indicated by a vertical line in the plots of Figure 10. All data from cold-rolled AA5083 materials show a small exotherm at approximately 300 °C, which is indicative of the recrystallization temperature (T_{RX}); this feature is naturally missing in the data from recrystallized samples. Data from material CC-B, shown in Figure 10(d), are unique in exhibiting incipient melting. Incipient melting occurs in material CC-B within a temperature range of 552 °C to 568 °C. This is shown in Figure 10(d) for a recrystallized sample, but identical behavior was also observed in a cold-rolled sample of material CC-B. Data from a full heating-and-cooling thermal cycle are presented in Figure 10(d). The data from controlled cooling exhibit an exotherm that is characteristic of solidification following incipient melting during the prior controlled heating. These data are consistent with the melting and solidification of a discrete phase, or phases, below the AA5083 solidus temperature.

Phase diagram data[26,27] for ternary Al-Cu-Mg alloys suggest that S phase (Al$_2$CuMg) will precipitate in the terminal Al solid solution during equilibrium cooling of a material having the Mg and Cu concentrations of material CC-B. Unfortunately, there is a general lack of data on the
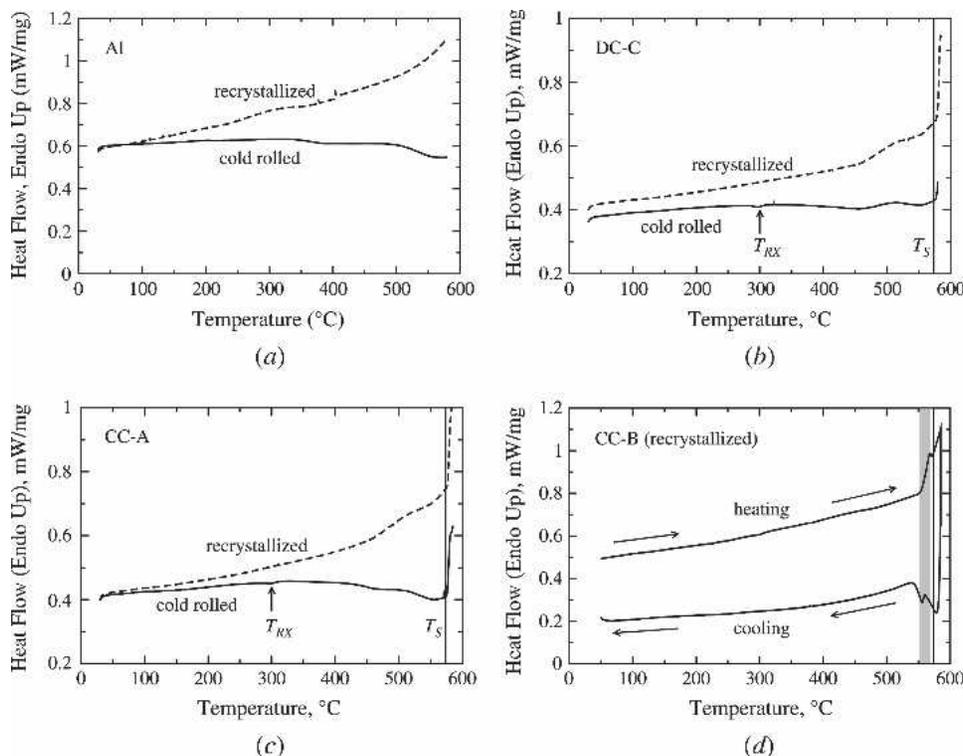

Fig. 10—Data from DSC experiments are shown as heat flow against temperature for (*a*) high-purity aluminum, (*b*) material DC-C, (*c*) material CC-A, and (*d*) material CC-B. The vertical line in plots (b), (c), and (d) indicates the solidus temperature of AA5083, and the gray region in (d) represents the range of temperatures from the $\beta + \gamma$ eutectic temperature to the β melting temperature.

S phase in Cu-lean Al-Mg-Cu alloys.[28,29] The Al_6CuMg_4 and Al_8Mg_5 phases may also form at lower temperatures. The S phase forms a quasi-binary eutectic with the Al solid solution, and the maximum solubility of S occurs at the eutectic temperature of 518 °C and 2.8Mg-3.0Cu, by weight. The effects of the Mn, Fe, and Si levels present in the CC-B material on the ternary Al-Cu-Mg phase diagram have not been determined. Nevertheless, interpolation of available ternary data indicate that for the CC-B composition of 4.7Mg-0.61Cu, the liquidus temperature is approximately 640 °C, the solidus is approximately 550 °C, and the solvus is approximately 440 °C. For an Al-4.7 Mg alloy, the maximum solubility of Cu is 1.7 wt pct at 508 °C, and a single-phase solid-solution region in the ternary diagram extends downward from the solidus temperature to the solvus temperature for the CC-B material. Of particular note is that the addition of 0.61 wt pct Cu to the nominal AA5083 composition apparently reduces the solidus temperature by approximately 25 °C, and the observed incipient melting temperature of CC-B is consistent with such a reduction. It should also be noted that the observed incipient melting range corresponds closely to the melting temperatures of the intermetallic $\beta(Mg_2Cu)$, 568 °C, and the β-γ ($MgCu_2$) eutectic, 552 °C, in the Cu-Mg system[30]; this range of temperatures is indicated by the shaded area in Figure 10(d). Thus, incipient melting of a β-rich mixture of the eutectic β-γ intermetallics is also consistent with the DSC

data, although these intermetallic phases are not necessarily expected from the Al-Cu-Mg ternary phase diagram.

The TEM analysis was conducted for each material in the recrystallized state in order to clarify microstructural differences suggested by the DSC data. Figure 11 shows typical photomicrographs for each of the three AA5083 materials. Prismatic particles distributed throughout the matrix were observed in all three cases, e.g., p2 in Figure 11(d), while platelike particles were observed at grain boundaries in the CC-B material, e.g., arrow in Figure 11(c) and p1 and p3 in Figure 11(d). Microanalysis data were acquired by EDS of the alloy matrix, e.g., M in Figure 11(d); the prismatic particles for each of these materials; and the platelike particles for the CC-B material. Results of EDS analysis for the CC-B material are presented in Figure 12. Aside from Al, only Mg and a small Cu peak are apparent in the EDS data for the alloy matrix, as illustrated in Figure 12(a), while prominent Cu and Mg peaks are apparent for the platelike particles on grain boundaries. The spectrum of the platelike particle denoted p1 in Figure 11(d) is shown in Figure 12(b), and these data indicate roughly equal parts of Cu and Mg. The platelike particles have diameters of approximately 150 nm, which is on the order of the foil thickness, but have thicknesses on the order of the nominal beam diameter, which was 6 nm. Because the platelike particles are thin in the plane of the grain boundary, the EDS data certainly include signals from
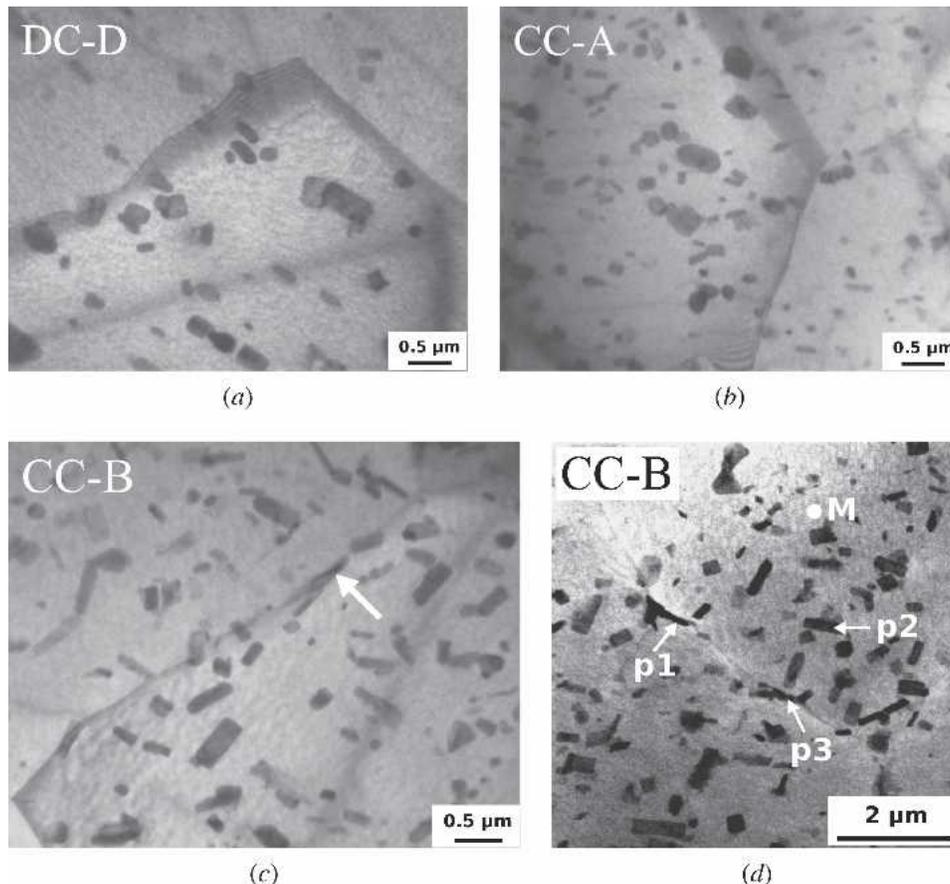

Fig. 11—TEM photomicrographs are shown for materials (a) DC-D, (b) CC-A, and (c) CC-B in the recrystallized state. (d) Points in material CC-B evaluated by EDS.
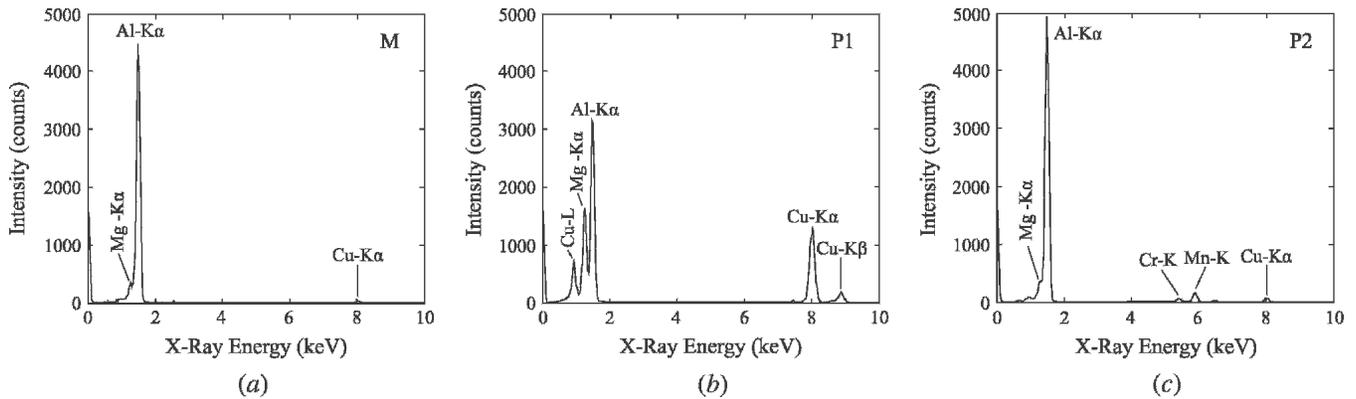
Fig. 12—Results of EDS analysis are shown for the CC-B material at various locations, as indicated in Fig. 11(d): (*a*) the alloy matrix at point M, (*b*) a platelike grain-boundary particle at point p1, and (*c*) a prismatic particle at point p2.

matrix material. Diffraction results could not be obtained from these particles. A typical prismatic particle contained Mn and gave some indication of Cr and also Cu in material CC-B as shown in Figure 12(c). These prismatic particles are the expected fine dispersion of Al_6Mn.

The equilibrium phase diagram data, the DSC data, and the TEM analysis indicate that incipient melting associated with the Cu addition to a nominal AA5083 composition is related to the platelike particles observed on grain boundaries in the CC-B material. These particles are likely *S* or its precursors. However, the present data cannot rule out the possibility that these particles are associated with the β-γ eutectic of the Cu-Mg system. The location of the platelike particles on grain boundaries suggests formation during deformation or upon cooling below the solvus temperature and may indicate segregation of the Cu solute to grain boundaries prior to precipitation. Segregation of Cu to grain boundaries is expected, from the phase diagram data, to locally reduce the solidus temperature and, thus, increase grain-boundary diffusivity. Such a mechanism of enhancing grain-boundary diffusion may explain the decreased flow stress, *i.e.,* faster creep rate, of the CC-B material under GBS creep deformation compared to the CC-A and DC-C materials.

IV. CONCLUSIONS

A Cu addition to a continuously cast material of nominally AA5083 composition is observed to produce a number of significant effects. The Cu addition reduces flow stress when deformation is by GBS creep, although grain size is not significantly affected. Activation energies for creep under both SD and GBS creep deformation mechanisms are similar between the Cu-containing CC-B material and AA5083 materials without a Cu addition. Creep transient data for the CC-B material indicate that Cu does not significantly affect transient creep in the SD creep regime. However, the Cu addition increases tensile ductility of the CC-B material at 450 °C beyond that of the CC-A material and introduces a temperature dependence for tensile ductility, with elongations decreasing as temperature increases from 450 °C to 500 °C. Despite its increased tensile ductility, the CC-B material exhibits cavitation under GBS

creep in a manner similar to that of material CC-A. This indicates that the Cu addition increases elongation to failure, but may not increase usable ductility in forming operations when cavitation is the limiting factor. The Cu addition in material CC-B does not result in significantly altered intermetallic particle-size-population densities between 1.5 and 7 μm, compared to the CC-A material. Failure surface features are unaltered by the Cu addition in material CC-B, which exhibits failure surfaces similar to the CC-A and DC-C materials. The DSC data indicate incipient melting in material CC-B from 552 °C to 568 °C, which is above the temperatures used in mechanical testing. The TEM and EDS data confirm the presence of platelike particles rich in Mg and Cu at grain boundaries in the CC-B material and the absence of such particles in the DC-C and CC-A materials. These particles are likely *S* phase, but were not positively identified as such. These platelike particles appear responsible for incipient melting observed in DSC data, a lowered flow stress under GBS creep, a higher tensile ductility of the CC-B material relative to material CC-A, and a strong temperature dependence for ductility and cavitation under GBS creep between 450 °C and 500 °C.

REFERENCES

1. F.J. Humphreys: *Acta Metall.*, 1977, vol. 25, pp. 1323-44.
2. F.J. Humphreys: *Met. Sci.*, 1979, vol. 13, pp. 136-45.
3. D. Doherty, D.A. Hughes, F.J. Humphreys, J.J. Jonas, D. Juul Jensen, M.E. Kassner, W.E. King, T.R. McNelley, H.J. McQueen, and A.D. Rollett: *Mater. Sci. Eng.*, 1997, vol. A238, pp. 219-74.
4. M.-A. Kulas, W.P. Green, E.M. Taleff, P.E. Krajewski, and T.R. McNelley: *Metall. Mater. Trans. A*, 2005, vol. 36A, pp. 1249-61.
5. M.-A. Kulas, W.P. Green, E.C. Pettengill, P.E. Krajewski, and E.M. Taleff: in *Advances in Superplasticity and Superplastic Forming,* E.M. Taleff, P.A. Friedman, P.E. Krajewski, R.S. Mishra, and J.G. Schroth, eds., TMS, Warrendale, PA, 2004, pp. 127-38.
6. M.-A. Kulas, W.P. Green, E.M. Taleff, P.E. Krajewski, and T.R. McNelley: *Metall. Mater. Trans. A*, 2005, vol. 36A, pp. 645-55.
7. D.H. Bae and A.K. Ghosh: *Acta Mater.*, 2002, vol. 50, pp. 511-23.
8. D.H. Bae, A.K. Ghosh, and J.R. Bradley: *Metall. Mater. Trans. A,* 2003, vol. 34A, pp. 2449-63.
9. E.M. Taleff, P.J. Nevland, and P.E. Krajewski: *Metall. Mater. Trans. A,* 2001, vol. 32A, pp. 1119-30.
10. J.G. Schroth: in *Advances in Superplasticity and Superplastic Forming,* E.M. Taleff, P.A. Friedman, P.E. Krajewski, R.S. Mishra, and J.G. Schroth, eds., TMS, Warrendale, PA, 2004, pp. 9-20.
11. H. Watanabe, K. Ohori, and Y. Takeuchi: *Trans. Iron Steel Inst. Jpn.*, 1987, vol. 27, pp. 730-3.

12. M.J. Starink: *Int. Mater. Rev.*, 2004, vol. 49, pp. 191-226.
13. "Standard Test Methods for Determining Average Grain Size." *ASTM Standard Designation E 112-96*, ASTM, West Conshohocken, PA, 1996.
14. http://rsb.info.nih.gov/ij/
15. W. Köster: *Z. Metallkd.*, 1948, vol. 39, pp. 1-9.
16. W. Köster: *Z. Metallkd.*, 1948, vol. 39, pp. 9-12.
17. K. Abe, Y. Tanji, H. Yoshinaga, and S. Morozumi: *J. Jpn. Inst. Light Met.*, 1977, vol. 27, pp. 279-81.
18. O.D. Sherby and J. Wadsworth: *Progr. Mater. Sci.*, 1989, vol. 33, pp. 169-221.
19. E.M. Taleff: in *Advances in Superplasticity and Superplastic Forming,* E.M. Taleff, P.A. Friedman, P.E. Krajewski, R.S. Mishra, and J.G. Schroth, eds., TMS, Warrendale, PA, 2004, pp. 85-94.
20. R. Lagneborg and B. Bergman: *Met. Sci.*, 1976, vol. 10, pp. 20-28.
21. J. Weertman: *J. Appl. Phys.*, 1957, vol. 28, pp. 1185-89.
22. J. Weertman: *Trans. TMS-AIME*, 1960, vol. 218, pp. 207-18.
23. O.D. Sherby and P.M. Burke: *Progr. Mater. Sci.*, 1968, vol. 13, pp. 325-90.
24. E.M. Taleff, W.P. Green, M.-A. Kulas, T.R. McNelley, and P.E. Krajewski: *Mater. Sci. Eng.*, 2005, vol. 36, pp. 1249-61.
25. *ASM Specialty Handbook: Aluminum and Aluminum Alloys,* J.R. David, ed., ASM INTERNATIONAL, Metals Park, OH, 1993, pp. 675-76.
26. *Metals Handbook,* 8th ed., T. Lyman, ed., ASM, Metals Park, OH, 1973, vol. 8, p. 386.
27. L.F. Mondolfo: *Aluminum Alloys: Structure and Properties,* Butterworth and Co., London, 1976, pp. 497-505.
28. V. Radmilovic, R. Kilaas, U. Dahmen, and G.J. Shiflet: *Acta Mater.*, 1999, vol. 47, pp. 3987-97.
29. L. Kovarik, P.I. Gouma, C. Kisielowski, S.A. Court, and M.J. Mills: *Acta Mater.*, 2004, vol. 52, pp. 2509-20.
30. *Metals Handbook,* 8th ed., T. Lyman, ed., ASM, Metals Park, OH, 1973, vol. 8, p. 294.